

General Working Principles of $\text{CH}_3\text{NH}_3\text{PbX}_3$ Perovskite Solar Cells

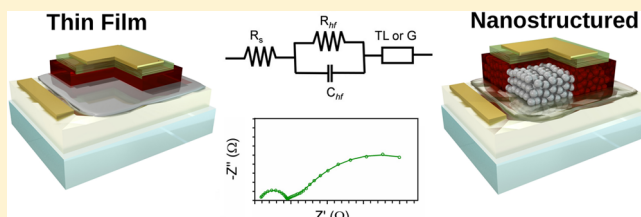
Victoria Gonzalez-Pedro,[†] Emilio J. Juarez-Perez,[†] Waode-Sukmawati Arsyad,[‡] Eva M. Barea, Francisco Fabregat-Santiago, Ivan Mora-Sero,* and Juan Bisquert*

Photovoltaics and Optoelectronic Devices Group, Departament de Fisica, Universitat Jaume I, 12071 Castello, Spain

Supporting Information

ABSTRACT: Organometal halide perovskite-based solar cells have recently realized large conversion efficiency over 15% showing great promise for a new large scale cost-competitive photovoltaic technology. Using impedance spectroscopy measurements we are able to separate the physical parameters of carrier transport and recombination in working devices of the two principal morphologies and compositions of perovskite solar cells, viz. compact thin films of $\text{CH}_3\text{NH}_3\text{PbI}_{3-x}\text{Cl}_x$ and $\text{CH}_3\text{NH}_3\text{PbI}_3$ infiltrated on nanostructured TiO_2 . The results show nearly identical spectral characteristics indicating a unique photovoltaic operating mechanism that provides long diffusion lengths ($1 \mu\text{m}$). Carrier conductivity in both devices is closely matched, so that the most significant differences in performance are attributed to recombination rates. These results highlight the central role of the $\text{CH}_3\text{NH}_3\text{PbX}_3$ semiconductor absorber in carrier collection and provide a new tool for improved optimization of perovskite solar cells. We report for the first time a measurement of the diffusion length in a nanostructured perovskite solar cell.

KEYWORDS: Semiconductor, perovskite, solar cells, photovoltaics



The necessity of cheap energy from a clean and abundant source has naturally stirred a large research effort to find low cost and high efficiency devices to convert sunlight to electricity. A range of solution processed organic and hybrid organic–inorganic solar cells,¹ such as dye-sensitized solar cells (DSC) and bulk heterojunction organic solar cells, have been intensely developed in the last two decades, but the conversion efficiencies required to compete in the energy market have not yet been realized. A recent newcomer to the field of solution-processed photovoltaics is the lead halide perovskite solar cell. It is based on organic–inorganic light absorbing semiconductor material with a perovskite polycrystalline structure, $\text{CH}_3\text{NH}_3\text{PbX}_3$, where X is a halide atom (I, Cl, Br, or a combination of some of them). This light harvester material has recently provoked a major progress starting with the work of Miyasaka et al.² who used it as a variant of the DSC configuration, thus a nanostructured TiO_2 perovskite-sensitized solar cell. Subsequently, the perovskite solar cells have been assembled in a variety of morphologies, either in nano-heterojunction or planar thin film, with different chemical compositions and preparation routes. Very quickly the promising initial results, with efficiencies between 10 and 12% at one sun equivalent illumination^{3–9} have passed to values exceeding 15%.^{10,11} These record efficiencies have been reported with two quite different configurations, using $\text{CH}_3\text{NH}_3\text{PbI}_3$ perovskite grown by a sequential solution method on nanostructured TiO_2 as in a classical DSC,¹⁰ and in a thin film configuration with $\text{CH}_3\text{NH}_3\text{PbI}_{3-x}\text{Cl}_x$ grown by vapor deposition.¹¹

The proficient operation of the $\text{CH}_3\text{NH}_3\text{PbX}_3$ perovskite solar cell that surprisingly has been accomplished by many

different approaches points to a robust photovoltaic operation mechanism that so far has not yet been fully understood. For further development of this field it is required to determine if there is a fundamental operational difference between thin film (TF) devices on the one hand and nanostructured devices (NS) including a metal oxide framework on the other. This raises the necessity for the knowledge of those physical electronic mechanisms that govern carrier separation, transport, extraction, and their recombination. An understanding of these processes and working principles is highly mandatory to assess the possibilities and properties of different materials, electrode contacts, and the overall device structure configuration. So far, very little information is available, and only in the absorber film, not in the whole operational devices.^{12,13} In this letter, we show that solar cell devices of different $\text{CH}_3\text{NH}_3\text{PbX}_3$ compositions in varying morphologies produce similar electro-optical spectral characteristics that are largely independent of the specific configuration. The results of impedance spectroscopy (IS) measurements provide essential information on carrier transport and recombination that enable unequivocal determination of cell conductivity and diffusion lengths larger than $1 \mu\text{m}$ at the working voltages of the solar cells.

Operating mechanisms of the organometal halide perovskite solar cells have raised a number of questions. As a reference, DSCs and bulk heterojunction organic solar cells take advantage of a nanostructured morphology that facilitates

Received: November 16, 2013

Revised: December 15, 2013

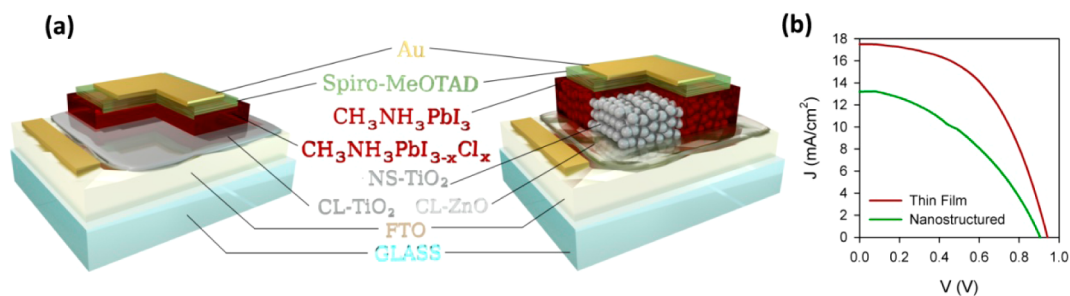


Figure 1. Solar cell configuration and performance. (a) Scheme and (b) J - V curves of the two different cell configurations analyzed: Thin film (TF), left, and nanostructured (NS), right.

Table 1. Solar Cell Parameters^a

sample	thickness (nm)	J_{sc} (mA/cm ²)	V_{oc} (V)	FF	η (%)	L_d (nm)
NS	585	13.2	0.908	0.41	4.9	~1000
TF	412	17.5	0.950	0.51	8.5	~1400
TF ^b	~400	15.4 ± 2.3	0.95 ± 0.05	0.47 ± 0.08	7.2 ± 1.2	

^aPhotovoltaic parameters of samples depicted in Figure 1. The cells analyzed correspond to the cells with the highest efficiency of each set. The average value and standard deviation of a set of 9 TF cells is added to highlight the reproducibility. Active layer thickness, short circuit current, J_{sc} , open circuit voltage, V_{oc} , fill factor, FF , photoconversion efficiency, η , and diffusion length at low applied bias. Solar cell parameters have been obtained from J - V curves without mask, and corrected taking into account the current obtained by integration of external quantum efficiency (EQE), producing an underestimation of efficiencies as discussed in the Methods section. ^b(Average + SD), $n = 9$.

rapid charge separation of photogenerated carriers to different materials. Ultrafast charge injection from the absorber to electron and hole transport materials, avoids recombination of electron-hole pairs and produces long diffusion lengths for effective charge collection. At the beginning of its discovery, the perovskite solar cell was a TiO₂ sensitized cell, so it was natural to believe that electrons would be injected to the wide bandgap metal oxide as the main transport pathway. However, the observation of significant efficiencies in perovskite solar cells with no electron transporting material,^{4,6} with no hole transporting material,¹⁴ or even in TF configuration^{11,15} indicates that perovskite solar cell can work in a sensibly different configuration than DSC. These results constitute a strong indication that photogenerated electrons and holes coexist in CH₃NH₃PbX₃ absorber material and travel to the selective contacts where they are separately collected. In this sense, a determination of important parameters for cell performance in terms of transport and recombination, namely, the conductivity, σ , and diffusion length, L_d , that have not yet been identified in working devices, constitutes a step forward to a further optimization of the solar cells.

With the aim of obtaining these parameters and to identify the possible similarities and differences between the main kinds of perovskite solar cells, we decided to investigate photovoltaic behavior of the two dominant cell configurations used so far, indicated in Figure 1a. The first is a planar thin film (TF) of mixed halide CH₃NH₃PbI_{3-x}Cl_x perovskite prepared by spin coating method⁶ over TiO₂ compact layer. The second type is a nanostructured (NS) device of CH₃NH₃PbI₃, prepared by sequential deposition method,¹⁰ in which TiO₂ is used as scaffold and compact ZnO as electron selective contact. The hole selective contact material is spiro-MeOTAD (2,2',7,7'-tetrakis-(*N,N*-di-*p*-methoxyphenylamine)-9,9'(spirobifluorene) in both cases. SEM micrographs of analyzed cells can be found in Figure S1, Supporting Information.

Figure 1b and Table 1 present the current density-voltage (J - V) curve and solar cell parameters, respectively, for NS and TF samples. Both cells show similar open circuit potential, V_{oc}

but the higher short circuit current, J_{sc} , and fill factor, FF , of TF cell produces a higher photoconversion efficiency, $\eta = 8.5\%$.

To determine the photovoltaic operation of the devices we used the measurement techniques that have become highly standard for the determination of main electronic processes in the working device conditions to a variety of inorganic and hybrid solar cells, including DSCs and quantum-dot sensitized solar cells, both with liquid electrolyte and all-solid configurations¹⁶⁻¹⁸ and also in conventional amorphous and crystalline silicon solar cells.^{19,20} The results of these techniques will be validated for the first time for the perovskite solar cell in this letter, although previously we have reported specific features of the capacitance.²¹

Figure 2 plots a set of the characteristic impedance spectra patterns obtained for both cells at different applied voltages in the working conditions under 1 sun illumination. For all the spectra an arc is observed at high frequencies. This arc is related to the transport in spiro-MeOTAD,²¹⁻²³ see Figure S2, Supporting Information. At low frequencies for TF sample the classical feature of a transmission line, TL, discussed below, is clearly visible. Note especially the insets that show clearly the turnover from the transport line of inclination $\sim 45^\circ$ to the low frequency arc. In the case of NS sample, the TL is also observed at $0 \leq V \leq 0.5$ V. These features unequivocally show the transport of the dominant carrier coupled with recombination along the whole active film thickness, as previously seen in theory and many experimental studies.²⁴ In the case of ambipolar transport, the transport features correspond to coupled electron-hole transport in ambipolar diffusion. Unfortunately it is not possible to infer the kind of carrier just from the impedance measurements since the electrical response is symmetrical for either electrons or holes. In any case, the measured parameters determine the relevant carrier for the photovoltaic action, which is the objective of this work, and more extended studies will be carried out in the near future for a more precise knowledge of the specific transport mode in working devices.

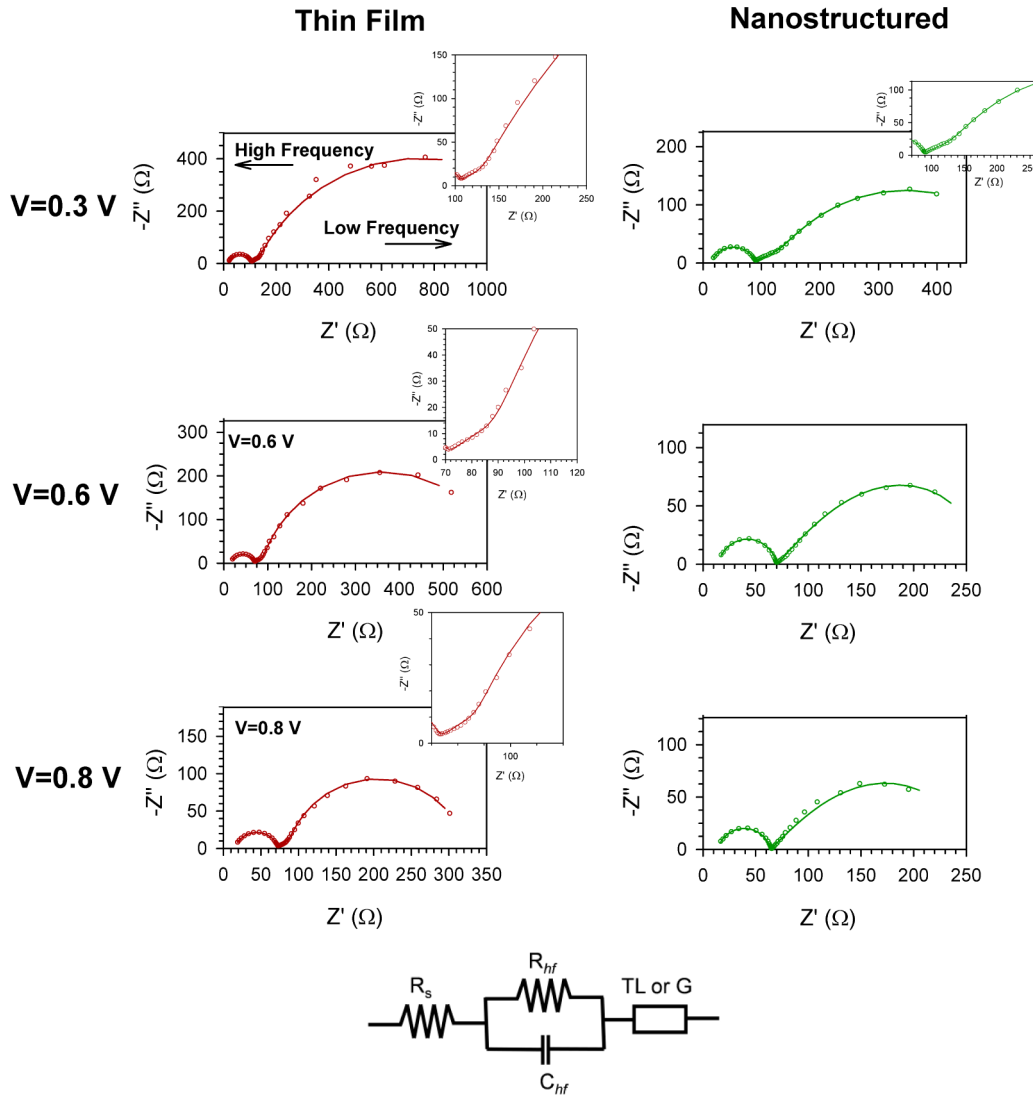


Figure 2. Impedance spectroscopy characterization. Complex plane impedance plots for thin film and nanostructured samples at different forward applied bias. Inset graphs are zooms showing the turnover from transport straight line to recombination arc. Symbols are the experimental results and solid lines correspond to the fit using the equivalent circuit depicted at the bottom. Depending on the impedance spectra pattern, a transmission line (TL) or Gerischer element (G) has been employed. G has been used in NS sample at $V > 0.5$ V and TL for the rest of conditions plotted in this figure. Low and high Frequency regions of the impedance spectra are indicated for clarity reasons in the top left graph.

In solar cells, a transport–recombination behavior produces the classical spectral feature of a transmission line, TL,^{16,25,26} that has been widely reported and used in DSCs.^{17,18,27} The TL pattern is defined by a straight line, associated to the carrier transport, followed by an arc at lower frequency, which is due to a coupling of capacitance with recombination. In a TL pattern, the extension of the straight line cuts the semicircle at low frequencies. The fitting of transmission line allows to separate the two resistive parameters, for an active film of area A and layer thickness L : the transport resistance, R_{tr} , that is reciprocal to the carrier conductivity, σ , as

$$R_{tr} = \frac{L}{A\sigma} \tag{1}$$

and the recombination resistance, R_{rec} , that relates to the recombination flux, j_{rec} as

$$R_{rec} = \frac{1}{A} \left(\frac{\partial j_{rec}}{\partial V} \right)^{-1} \tag{2}$$

From these parameters the carrier diffusion length is given by^{16,26}

$$L_d = \left(\frac{R_{rec}}{R_{tr}} \right)^{1/2} L \tag{3}$$

The TL pattern is observed only when $R_{tr} < R_{rec}$, i.e., $L_d > L$, indicating efficient charge collection.^{16,26} In the case of NS sample the TL pattern is lost for applied voltage higher than 0.5 V, at forward applied bias. In those cases the extension of the straight line does not cut the semicircle at low frequencies, as the arc lays below the straight line, and a Gerischer (G) pattern is observed.²⁶ The appearance of the G pattern, determined by $R_{tr} > R_{rec}$ is quite significant as it indicates that L_d becomes shorter than L . Consequently, charge photogenerated along the whole sample cannot be totally collected. In addition in the G case, R_{rec} and R_{tr} cannot be unambiguously determined, just Gerischer resistance, R_G , can be obtained, as the recombination resistance of the region from which it is possible to collect

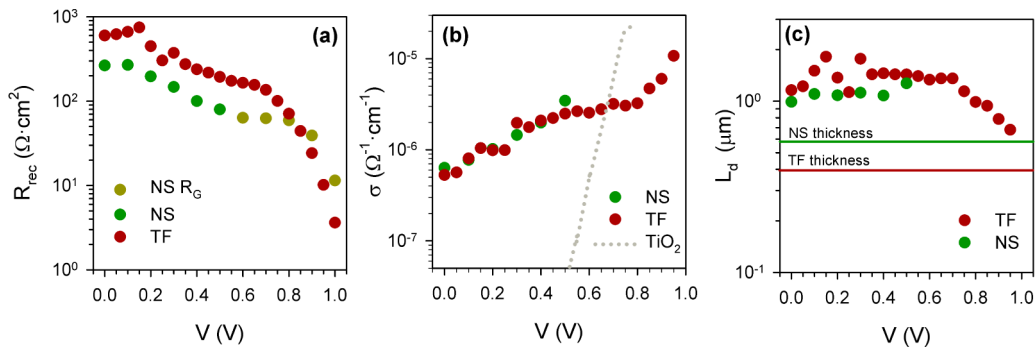


Figure 3. Transport and recombination parameters vs voltage: (a) recombination resistance, R_{rec} , (b) conductivity of active layer considering the geometric cell area, showing also the conductivity of nanostructured TiO_2 in a DSC with spiro-MeOTAD hole conductor, and (c) diffusion length for NS and TF cells. R_{tr} and R_{rec} cannot be unambiguously defined when Gerischer pattern is observed (NS sample for $V > 0.5$ V).

charge, and this region will be thinner than thickness of the sample.²⁶

To further determine the physical properties of the solar cells we have obtained the different parameters from the spectra. The fitting lines are shown in Figure 2, and the resulting parameters are presented in Figure 3. It is also worthy to note that more complex impedance spectra pattern have been observed in other cases,^{8,21} and we are currently working in a more general model encompassing all the cases, but it is significant to discuss the impedance in terms of clearly defined patterns as TL or G, plainly observed in Figure 2.

A prominent feature of the IS spectra for both cells is the similarity of the spectral shapes, despite the clear differences between devices, suggesting a unique and general transport–recombination mechanism. Since one of them does not have any metal oxide nanostructured framework, we must attribute the observed pattern to the perovskite absorber. This important point is confirmed by the calculation of carrier dc conductivity, see Figure 3b, from the transport resistance, using eq 1, that shows very similar values and voltage-dependence in both cells, see Figure S3, Supporting Information. At low voltage the conductivity values measured in NS and TF perovskite cells are orders of magnitude larger than that of nanostructured TiO_2 in a DSC, see also Figure S4, Supporting Information. In addition, the conductivity values at $V = 0$ are in good agreement with the values reported in the literature for polycrystalline $\text{CH}_3\text{NH}_3\text{PbI}_3$,^{28,29} which strongly supports our interpretation of the impedance spectra.

Important information about the recombination in the solar cell is contained in the recombination resistance, R_{rec} , depicted in Figure 3a, and we observe that NS sample presents lower resistance (higher recombination rate) than TF at low voltage. Since the transport rate is similar in both cells, the difference in recombination rate is an important feature to explain the different performance. However, close to the open circuit potential recombination is similar, and close values of V_{oc} are observed for both samples.

The central solar cell parameter L_d is now straightforwardly derived from eq 3. Here, we report for the first time a measurement of the diffusion length in complete perovskite solar cell, see Figure 3c. At low voltages L_d is practically constant, at strong variance with the well-known behavior in DSC where L_d increases with voltage.^{30,31} In the case of TF at low voltage $L_d \approx 1.4 \mu\text{m}$, while for $V > 0.7$ V, L_d decreases monotonically with the applied voltage but still with a value larger than L , indicating excellent charge collection capability. In the case of NS sample, that exhibits lower efficiency, L_d is

lower than in the case of TF in all the voltage range. At low voltage, $V \leq 0.5$ V, $L_d \approx 1 \mu\text{m}$, while at higher voltage, $V \geq 0.6$ V, it cannot be determined, as Gerischer feature appears, but in any case, it is lower than the layer thickness (~ 580 nm, see Figure S1, Supporting Information).²⁶ Since the conductivity is nearly the same for both cells, the lower diffusion length for the NS sample must be ascribed to the lower recombination resistance or larger recombination rate that has been noted above. The short diffusion length observed, in comparison with DSCs, even for cells with efficiency higher than 8%, explains the low performance observed for devices with active layer thicker than 400–600 nm.^{3,6}

L_d obtained for TF $\text{CH}_3\text{NH}_3\text{PbI}_{3-x}\text{Cl}_x$ perovskite solar cell is in good agreement with the diffusion length obtained for electrons and holes, between 1000 and 1200 nm, using photoluminescence (PL) quenching of thin films.¹² However, L_d obtained for TF $\text{CH}_3\text{NH}_3\text{PbI}_3$ by the same method is 1 order of magnitude lower,^{12,13} explaining why TF solar cells with $\text{CH}_3\text{NH}_3\text{PbI}_{3-x}\text{Cl}_x$ reports higher efficiency than TF $\text{CH}_3\text{NH}_3\text{PbI}_3$ devices. Nevertheless, our results show that a major increase of the L_d occurs when nanostructured TiO_2 framework is employed, in comparison with $\text{CH}_3\text{NH}_3\text{PbI}_3$ TF, to values over the micrometer, see Figure 3b. This fact explain why NS $\text{CH}_3\text{NH}_3\text{PbI}_3$ solar cells can attain more similar efficiencies than TF $\text{CH}_3\text{NH}_3\text{PbI}_{3-x}\text{Cl}_x$,^{10,11} indicating that NS layer may be necessary to enhance the L_d of $\text{CH}_3\text{NH}_3\text{PbI}_3$. We have prepared TF cells with $\text{CH}_3\text{NH}_3\text{PbI}_3$ perovskite and no nanoporous scaffold, using the same preparation method that for NS cells. The amount of perovskite deposited is sensibly lower than in the case of $\text{CH}_3\text{NH}_3\text{PbI}_{3-x}\text{Cl}_x$, as we have already pointed out in a previous work,²¹ and the efficiency is also significantly reduced, $<1\%$, see Figure S5, Supporting Information. As expected for low quality cells the TL impedance pattern is not visible for those samples, see Figure S5, Supporting Information, preventing the calculation of L_d in this case.

In conclusion, we have observed the transport coupled with recombination process in perovskite solar cells by the standard signature of transmission line pattern in the IS spectra. Despite the conspicuous differences of the samples in terms of perovskite material, growth method, sample configuration (nanostructured and thin film), or selective contact to electron, similar behavior has been observed indicating a common and general working mechanism in perovskite solar cells. The observation of TL allowed us to determine important cell parameters as carrier conductivity, recombination resistance, and diffusion length. The transport rate is nearly the same in

the different cells indicating that the dominant transport pathway is the perovskite absorber. The diffusion length plays a key role in the photovoltaic performance of perovskite solar cells, limiting the active layer thickness to few hundreds of nm. We found that a large diffusion length is achieved in compact film of $\text{CH}_3\text{NH}_3\text{PbI}_{3-x}\text{Cl}_x$, while the metal oxide nanostructure increases the L_d of $\text{CH}_3\text{NH}_3\text{PbI}_3$ perovskite. The model discussed in this work is highly consistent basically by three facts: (i) there are many physical processes producing an arc in an impedance spectra, but the observation of the straight line feature clearly indicates the presence of a transmission line or Gerischer impedance, which recognizes coupled transport and recombination and separates the correspondent resistance elements, as we discussed. (ii) Diffusion lengths obtained applying our model are in good agreement with the measured ones for thin film $\text{CH}_3\text{NH}_3\text{PbI}_{3-x}\text{Cl}_x$ measured by a completely different technique (time-resolved photoluminescence).¹² (iii) Perovskite conductivities applying our model are in good agreement with the previously reported ones, also measured by completely different techniques.^{28,29} The results here reported will contribute to the development of a complete model of the working principles in perovskite solar cells and could have important implications in the optimization and characterization of this technology.

Methods. Device Preparation. All the studied substrates were prepared over FTO (Pilkington TEC15, 15 Ω/sq resistance), which were previously etched with zinc powder and HCl (2 M) to obtain 0.224 cm^2 of active electrode area per pixel. The FTOs substrates were cleaned with soap (Hellmanex), deionized water, and ethanol, followed by sonication in a mixture acetone/water (v/v = 1:1). Before the deposition of electron selective contacts, substrates were treated in a UV-O₃ chamber for 15 min.

The substrates studied include flat TiO₂ and flat ZnO plus mesoporous TiO₂ as electron selective contacts. The TiO₂ compact layer was deposited on the clean substrates by aerosol spray pyrolysis at 500 °C using 40 mL of a titanium diisopropoxidebis(acetylacetonate) solution (75% in 2-propanol, Sigma-Aldrich) diluted in ethanol (1:39, v/v) and dinitrogen as carrier gas, and sintered on a hot plate for 1 h at 500 °C. The ZnO compact layer was prepared as it is described in ref 32, where an undoped ZnO compact layer was deposited on the clean substrates by spin coating (1000 rpm, 30 s) a 100 μL portion of a zinc acetate dihydrate solution in methanol (0.25 M). After drying at 100 °C during 15 min, the ZnO films were gradually heated to 500 °C for 1 h and cooled to room temperature. The TiO₂ compact layer thickness determined by scanning electron microscopy was ~ 50 nm. Porous TiO₂ films 568 nm thick were deposited onto ZnO substrates by spin coating at 1000 rpm during 30 s using a TiO₂ paste (Dyesol 18NRT, 20 nm average particle size) diluted in terpineol (1:3, weight ratio). After drying at 80 °C, the TiO₂ layers were heated to 470 °C for 15 min.

The perovskite absorber layer includes the study of $\text{CH}_3\text{NH}_3\text{PbI}_3$ halide perovskite and $\text{CH}_3\text{NH}_3\text{PbI}_{3-x}\text{Cl}_x$ mixed halide perovskite. Both methodologies employ methylammonium iodide salt, which was previously synthesized following the procedure detailed elsewhere.⁴ The full iodide perovskite was deposited using the two-step sequential deposition method.¹⁰ In this procedure, PbI_2 was dissolved in *N,N*-dimethylformamide at a concentration of 33% (w/w) stirring at 80 °C and keeping it at 80 °C during the whole procedure. The mesoporous TiO₂ electrodes were then spin-coated with the

PbI_2 solution at 6500 rpm during 90 s and dried at 80 °C for 30 min. After cooling to room temperature, the films were dipped in a solution of $\text{CH}_3\text{NH}_3\text{I}$ in 2-propanol (10 mg/mL) for 30 s, rinsed with 2-propanol, and dried at 80 °C during 30 min. The mixed halide perovskite was prepared by spin coating procedure as reported in ref 15. In this methodology, 100 μL of perovskite precursor, 40% DMF solution of $\text{CH}_3\text{NH}_3\text{I}$, and PbCl_2 (3:1 molar ratio) was dispensed onto flat TiO₂ substrates and spin coated at 2000 rpm for 60 s. Then the films were placed on a hot plate at 100 °C for 10 min. All this procedure was performed in the glovebox. Finally the substrates were heated in furnace at 100 °C under air stream.

The perovskite-adsorbed films were covered with HTM layer by spin coating at 4000 rpm for 30 s outside of the glovebox. The HTM recipe was prepared dissolving 72.3 mg of (2,2',7,7'-tetrakis(*N,N*-di-*p*-methoxyphenylamine)-9,9-spirobifluorene) (spiro-MeOTAD), 28.8 μL of 4-*tert*-butylpyridine, and 17.5 μL of a stock solution of 520 mg/mL lithium bis-(trifluoromethylsulfonyl)imide in acetonitrile in 1 mL of chlorobenzene. Finally, 60 nm of gold was thermally evaporated in the vacuum chamber on top of the device to form the electrode contacts. The device fabrication was carried out under controlled atmospheric conditions and a humidity of <0.5 ppm, and the HTM layer deposition was carried out at room conditions.

Samples Characterization. Current–voltage curves were recorded under AM 1.5 100 mW/cm^2 simulated sunlight (ABET Technologies Sun 2000) with a Keithley 2400, previously calibrated with an NREL-calibrated Si solar cell. The measurements were performed without mask. The external quantum efficiency (EQE) measurements were performed employing a 150 W Xe lamp coupled with a monochromator controlled by a computer; the photocurrent was measured using an optical power meter 70310 from Oriel Instruments, using a Si photodiode to calibrate the system. Solar cell parameters reported in Table 1 and J – V curve have been corrected taking into account EQE analysis, in order to make coincident the J_{sc} obtained in both cases, see Figure S6, Supporting Information. This correction avoids to report overestimated J_{sc} when no mask is utilized in J – V characterization, as the high conductivity of the perovskites produces significant current that is transported laterally through the perovskite before being collected at the electrodes. However, this correction does not take into account the benefit of lower surface area, when mask is used, as obtaining higher FF. Consequently, this procedure introduces an underestimation of $\sim 10\%$ of power conversion efficiencies. Impedance spectroscopy measurements were carried out by means of a FRA equipped PGSTAT-30 from Autolab, under dark and illumination conditions and at different forward biases, by applying a 30 mV voltage perturbation over the constant forward applied bias, between 0 and 1 V, with the frequency ranging between 400 kHz and 0.05 Hz. Structural characterization of the samples was carried out by a JSM-7000F JEOL 216 FEG-SEM system.

■ ASSOCIATED CONTENT

📄 Supporting Information

SEM micrographs, impedance plots, conductivity vs voltage plots, J – V curves, and EQE analysis. This material is available free of charge via the Internet at <http://pubs.acs.org>.

AUTHOR INFORMATION

Corresponding Authors

*(I.M.-S.) E-mail: sero@uji.es.

*(J.B.) E-mail: bisquert@uji.es.

Present Address

‡(W.-S.A.) Bandung Institute of Technology, Ganesha 10, 40132, West Java, Indonesia

Author Contributions

†V.G.-P. and E.J.J.-P. have contributed equally to this work.

Notes

The authors declare no competing financial interest.

ACKNOWLEDGMENTS

We thank the following agencies for supporting this research: GeneralitatValenciana (ISIC/2012/008) and Universitat Jaume I project 12I361.01/1. We thank SCIC from Universitat Jaume I for the help with SEM measurements.

REFERENCES

- Grätzel, M.; Janssen, R. A. J.; Mitzi, D. B.; Sargent, E. H. *Nature* **2012**, *488* (7411), 304–312.
- Kojima, A.; Teshima, K.; Shirai, Y.; Miyasaka, T. *J. Am. Chem. Soc.* **2009**, *131*, 6050–6051.
- Kim, H.-S.; Lee, C.-R.; Im, J.-H.; Lee, K.-B.; Moehl, T.; Marchioro, A.; Moon, S.-J.; Humphry-Baker, R.; Yum, J.-H.; Moser, J. E.; Gratzel, M.; Park, N.-G. *Sci. Rep.* **2012**, *2*, 591.
- Lee, M. M.; Teuscher, J.; Miyasaka, T.; Murakami, T. N.; Snaith, H. J. *Science* **2012**, *338*, 643–647.
- Noh, J. H.; Im, S. H.; Heo, J. H.; Mandal, T. N.; Seok, S. I. *Nano Lett.* **2013**, *7*, 1764–1769.
- Ball, J. M.; Lee, M. M.; Hey, A.; Snaith, H. J. *Energy Environ. Sci.* **2013**, *6*, 1739–1743.
- Heo, J. H.; Im, S. H.; Noh, J. H.; Mandal, T. N.; Lim, C.-S.; Chang, J. A.; Lee, Y. H.; Kim, H.-J.; Sarkar, A.; Nazeeruddin, M. K.; Gratzel, M.; Seok, S. I. *Nat. Photonics* **2013**, *7*, 486–491.
- Kim, H.-S.; Lee, J.-W.; Yantara, N.; Boix, P. P.; Kulkarni, S. A.; Mhaisalkar, S.; Gratzel, M.; Park, N.-G. *Nano Lett.* **2013**, *16*, 2412–2417.
- Park, N.-G. *J. Phys. Chem. Lett.* **2013**, *4* (15), 2423–2429.
- Burschka, J.; Pellet, N.; Moon, S.-J.; Humphry-Baker, R.; Gao, P.; Nazeeruddin, M. K.; Gratzel, M. *Nature* **2013**, *499*, 316–319.
- Liu, M.; Johnston, M. B.; Snaith, H. J. *Nature* **2013**, *501*, 395–398.
- Stranks, S. D.; Eperon, G. E.; Grancini, G.; Menelaou, C.; Alcocer, M. J. P.; Leijtens, T.; Herz, L. M.; Petrozza, A.; Snaith, H. J. *Science* **2013**, *342* (6156), 341–344.
- Xing, G.; Mathews, N.; Sun, S.; Lim, S. S.; Lam, Y. M.; Gratzel, M.; Mhaisalkar, S.; Sum, T. C. *Science* **2013**, *342*, 344–347.
- Etgar, L.; Gao, P.; Xue, Z.; Peng, Q.; Chandiran, A. K.; Liu, B.; Nazeeruddin, M. K.; Grätzel, M. *J. Am. Chem. Soc.* **2012**, *134*, 17396–17399.
- Eperon, G. E.; Burlakov, V. M.; Docampo, P.; Goriely, A.; Snaith, H. J. *Adv. Funct. Mater.* **2014**, *24*, 151–157.
- Bisquert, J. *J. Phys. Chem. B* **2002**, *106*, 325–333.
- Fabregat-Santiago, F.; Bisquert, J.; Garcia-Belmonte, G.; Boschloo, G.; Hagfeldt, A. *Sol. Energy Mater. Sol. Cells* **2005**, *87*, 117–131.
- Wang, Q.; Ito, S.; Grätzel, M.; Fabregat-Santiago, F.; Mora-Seró, I.; Bisquert, J.; Bessho, T.; Imai, H. *J. Phys. Chem. B* **2006**, *110*, 19406–19411.
- Mora-Seró, I.; Luo, Y.; Garcia-Belmonte, G.; Bisquert, J.; Muñoz, D.; Voz, C.; Puigdollers, J.; Alcubilla, R. *Sol. Energy Mater. Sol. Cells* **2008**, *92*, 505–509.
- Mora-Seró, I.; Garcia-Belmonte, G.; Boix, P. P.; Vázquez, M. A.; Bisquert, J. *Energy Environ. Sci.* **2009**, *2*, 678–686.
- Kim, H.-S.; Mora-Sero, I.; Gonzalez-Pedro, V.; Fabregat-Santiago, F.; Juarez-Perez, E. J.; Park, N.-G.; Bisquert, J. *Nat. Commun.* **2013**, *4*, 2242.
- Fabregat-Santiago, F.; Bisquert, J.; Cevey, L.; Chen, P.; Wang, M.; Zakeeruddin, S. M.; Grätzel, M. *J. Am. Chem. Soc.* **2009**, *131*, 558–562.
- Dualeh, A.; Moehl, T.; Nazeeruddin, M. K.; Grätzel, M. *ACS Nano* **2013**, *7*, 2292–2301.
- Jennings, J. R.; Liu, Y.; Safari-Alamuti, F.; Wang, Q. *J. Phys. Chem. C* **2012**, *116*, 1556–1562.
- Bisquert, J.; Garcia-Belmonte, G.; Fabregat-Santiago, F.; Ferriols, N. S.; Bogdanoff, P.; Pereira, E. C. *J. Phys. Chem. B* **2000**, *104*, 2287–2298.
- Bisquert, J.; Mora-Sero, I.; Fabregat-Santiago, F. *ChemElectroChem* **2013**, DOI: 10.1002/celc.201300091.
- Fabregat-Santiago, F.; Garcia-Belmonte, G.; Mora-Seró, I.; Bisquert, J. *J. Phys. Chem. Chem. Phys.* **2011**, *13*, 9083–9118.
- Knop, O.; Wasylshen, R. E.; White, M. A.; Cameron, T. S.; Oort, M. J. M. V. *Can. J. Chem.* **1990**, *68*, 412–422.
- Stoumpos, C. C.; Malliakas, C. D.; Kanatzidis, M. G. *Inorg. Chem.* **2013**, *52*, 9019–9038.
- Jennings, J. R.; Liu, Y.; Safari-Alamuti, F.; Wang, Q. *J. Phys. Chem. C* **2011**, *116*, 1556–1562.
- Bisquert, J.; Mora-Seró, I. *J. Phys. Chem. Lett.* **2010**, *1*, 450–456.
- Aprilia, A.; Wulandari, P.; Suendo, V.; Herman; Hidayat, R.; Fujii, A.; Ozaki, M. *Sol. Energy Mater. Sol. Cells* **2013**, *111*, 181–188.